CDDpress

www.nature.com/cddis

ARTICLE OPEN

Mechano-inhibition of endocytosis sensitizes cancer cells to Fas-induced Apoptosis

Mehmet H. Kural[1,7,9✉], Umidahan Djakbarova[2,9], Bilal Cakir[3], Yoshiaki Tanaka[3,8], Emily T. Chan[2,4], Valeria I. Arteaga Muniz[2], Yasaman Madraki[2], Hong Qian[1,7], Jinkyu Park[5], Lorenzo R. Sewanan[6], In-Hyun Park[3], Laura E. Niklason[1,7✉] and Comert Kural[2,4✉]

The transmembrane death receptor Fas transduces apoptotic signals upon binding its ligand, FasL. Although Fas is highly expressed in cancer cells, insufficient cell surface Fas expression desensitizes cancer cells to Fas-induced apoptosis. Here, we show that the increase in Fas microaggregate formation on the plasma membrane in response to the inhibition of endocytosis sensitizes cancer cells to Fas-induced apoptosis. We used a clinically accessible Rho-kinase inhibitor, fasudil, that reduces endocytosis dynamics by increasing plasma membrane tension. In combination with exogenous soluble FasL (sFasL), fasudil promoted cancer cell apoptosis, but this collaborative effect was substantially weaker in nonmalignant cells. The combination of sFasL and fasudil prevented glioblastoma cell growth in embryonic stem cell-derived brain organoids and induced tumor regression in a xenograft mouse model. Our results demonstrate that sFasL has strong potential for apoptosis-directed cancer therapy when Fas microaggregate formation is augmented by mechano-inhibition of endocytosis.

Cell Death and Disease (2024)15:440 ; https://doi.org/10.1038/s41419-024-06822-3

INTRODUCTION

Fas (CD95/APO-1) is a death receptor in the tumor necrosis factor (TNF) superfamily that regulates immune system homeostasis [1]. The physiologic ligand of Fas, FasL, is a type II transmembrane protein expressed on the surface of activated T cells and natural killer cells [2]. These cells can also secrete a soluble form of FasL (sFasL) that lacks the transmembrane domain and is therefore able to circulate freely in the bloodstream [3]. Upon ligation at the plasma membrane, Fas clusters form and generate the death-inducing signaling complex (DISC), which activates caspase-8 to initiate a downstream signaling cascade that leads to apoptosis [2, 4]. Intracellular Fas trafficking, including recycling via endosomes to the plasma membrane, plays a vital role in ligand-induced DISC assembly [5, 6].

Since Fas expression is associated with increased cell proliferation and metastasis in numerous types of cancer, there have been several attempts to target Fas-mediated apoptosis to specifically kill tumor cells [7–15]. However, the development of a systemic therapy utilizing sFasL has thus far failed because sFasL alone has weak apoptosis-inducing capacity in vivo [8], and most human tumors are desensitized to Fas-induced apoptosis [14, 16]. Attempts to increase the efficacy of sFasL using cross-linking antibodies resulted in systemic toxicity in mice [8]. Thus, novel approaches to targeting the Fas-mediated apoptosis pathway are needed to take advantage of differences in Fas expression and signaling between cancer and normal cells.

The aggregation of Fas receptors in the plasma membrane increases the efficiency of DISC formation upon FasL stimulation [17, 18]. As Fas levels below the threshold for ligand-induced clustering render cancer cells insensitive to Fas-induced apoptosis [6, 19–21], cancer cells have adopted distinct strategies to reduce Fas surface levels. For example, in tumor cells lacking functional p53, Fas is not transported from the Golgi complex to the plasma membrane [22]. Moreover, Fas molecules endocytosed from the cancer cell surface are predominantly delivered to lysosomes for degradation, not recycled to the plasma membrane [6]. Therefore, we aimed to determine whether slowing the endocytic machinery decreases Fas internalization and increases Fas density at the plasma membrane, ultimately increasing the susceptibility of cancer cells to Fas-induced apoptosis in the presence of sFasL through activation of the caspase cascade (Fig. 1a).

Cells utilize endocytosis machinery to transform flat membrane patches into highly curved endocytic pockets and vesicles [23–26]; such curvature generation is hindered by mechanical tension on the plasma membrane, a potent and reversible regulator of endocytosis dynamics in cells [26–30]. Increasing membrane tension is one way to disrupt endocytosis and thus significantly alter the plasma membrane proteome [31, 32],

[1]Department of Anesthesiology, School of Medicine, Yale University, New Haven, CT 06519, USA. [2]Department of Physics, The Ohio State University, Columbus, OH 43210, USA. [3]Department of Genetics, Yale Stem Cell Center, Yale School of Medicine, New Haven, CT 06519, USA. [4]Interdisciplinary Biophysics Graduate Program, The Ohio State University, Columbus, OH 43210, USA. [5]Yale Cardiovascular Research Center, Department of Internal Medicine, School of Medicine, Yale University, New Haven, CT 06519, USA. [6]Department of Internal Medicine, Columbia University, New York, NY 10032, USA. [7]Present address: Humacyte Inc., Durham, NC 27213, USA. [8]Present address: Department of Medicine, Maisonneuve-Rosemont Hospital Research Center, University of Montreal, Montreal, QC H1T 2M4, Canada. [9]These authors contributed equally: Mehmet H. Kural, Umidahan Djakbarova. ✉email: mkural@humacyte.com; niklason@humacyte.com; kural.1@osu.edu

Edited by Mauro Piacentini

Received: 8 December 2023 Revised: 4 June 2024 Accepted: 10 June 2024
Published online: 22 June 2024

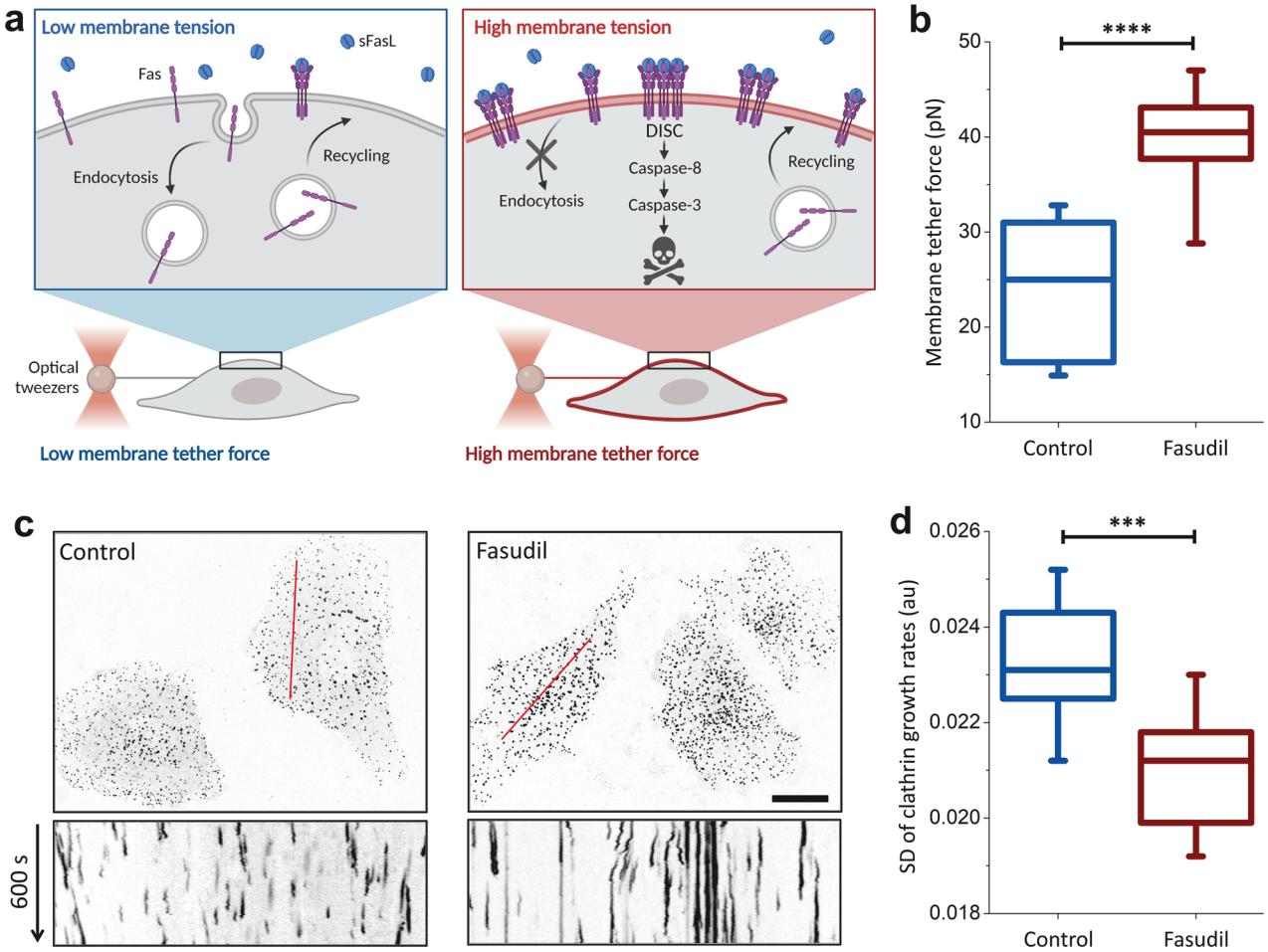

Fig. 1 Mechano-inhibition of endocytosis by fasudil. a Schematic representation of the study hypothesis: internalization of Fas from the cell surface reduces the sensitivity of cancer cells to Fas-induced apoptosis. Inhibition of endocytosis pathways is expected to increase Fas expression on the cell surface and enhance the formation of the death-inducing signaling complex (DISC) in the presence of sFasL. Endocytosis is slowed by increasing plasma membrane tension, which can be quantified using optical tweezers to measure the membrane tether force. **b** SUM159 cells treated with 40 μM fasudil showed significantly higher membrane tension than did untreated cells. $N_{cells} = 19$ (untreated) and 28 (fasudil). **c** Endocytic clathrin coats were imaged at the ventral surface of live SUM159 cells (genome edited to express AP2-EGFP) that were untreated (left) or treated with 40 μM fasudil for two hours (right). Kymographs obtained along the marked regions show clathrin-mediated endocytosis dynamics, with short streaks representing fast endocytic events. Streak length increased as endocytosis dynamics slowed. Fluorescence images are inverted to increase visibility. **d** Standard deviation (SD) of the clathrin growth rates significantly reduced after treatment with 40 μM fasudil. $N_{cells} = 14$, $N_{events} = 84230$. ****$p < 0.0001$, ***$p < 0.001$; two-tailed t test. Scale bar, 20 μm.

thereby regulating various cellular and organismal processes [31, 33–35]. Interestingly, the membrane tension of cancer cells is significantly lower than that of their nonmalignant counterparts [36–38]. Although lower membrane tension may set the stage for dysregulated endocytosis that contributes to malignant progression [39, 40], cancer cells are likely more susceptible to perturbations that impede endocytosis dynamics by elevating membrane tension [37, 38]. In this study, we show that fasudil [41], a clinically used Rho-kinase inhibitor, inhibits endocytosis in cancer cells by increasing plasma membrane tension. In support of our hypothesis, we found that inhibition of endocytosis increased the formation of Fas microaggregates on the cell surface and, thereby rendering cancer cells susceptible to Fas-induced apoptosis in the presence of sFasL. We further show that this strategy can be used to prevent glioblastoma growth in cortical organoids and mouse xenografts. Taken together, these results demonstrate that tumors can be targeted by Fas-induced apoptosis through the application of sFasL in combination with agents that reduce endocytosis dynamics and increase the formation of Fas microaggregates.

RESULTS

Reduced actomyosin contractility by fasudil leads to mechano-inhibition of endocytosis

Mechano-inhibition of endocytosis is characterized in cultured cells using techniques that allow modulation of plasma membrane tension, such as cell stretching [27, 42], aspiration [43], squeezing [28], and hypo-osmotic swelling [27, 28]. Although these approaches are effective in vitro, they are not suitable for systemic inhibition of endocytosis. Alternatively, reduced actomyosin contractility has been proposed to increase membrane tension by increasing the adhesion between the plasma membrane and the underlying actin cortex [44]. Correspondingly, we found that inhibition of the Rho-kinase by 40 μM fasudil treatment increased actin localization in the cell cortex (Supplementary Fig. 1a–d). The interaction between plasma membrane phospholipids and proteins and the underlying cortical actin is mediated by ezrin-radixin-moesin (ERM) family of proteins, known regulators of membrane tension [38, 45, 46]. Indeed, we found that fasudil treatment increased the peripheral localization of phosphorylated ERM along with actin (Supplementary Fig. 1e, f). Additionally, by

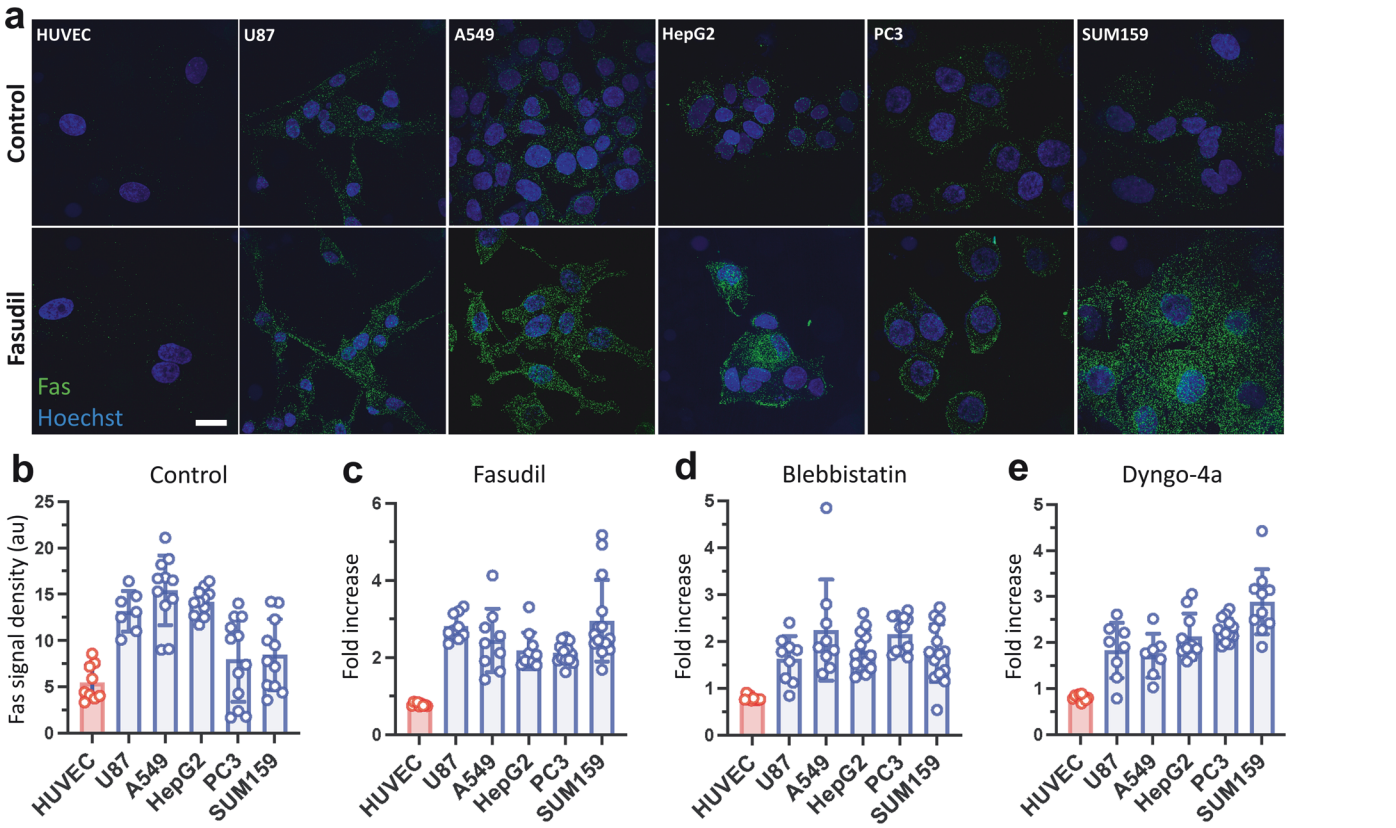

Fig. 2 Inhibition of endocytosis increases Fas microaggregate density on the cell surface. a Immunofluorescence assays show Fas microaggregate formation on HUVEC cells along with the cancerous U87, A549, HepG2, PC3 and SUM159 cells treated without (upper panel) or with fasudil (lower panel). **b** The density of the Fas signal is quantified by measuring the integrated microaggregate fluorescence per cell area. Fas signal density is shown for different cells in the absence of endocytosis inhibition. **c**–**e** Relative change in Fas signal density is shown for different cells after treatment with 40 μM fasudil (**c**), 10 μM blebbistatin (**d**), or 5 μM dyngo-4a (**e**) for 2 h. Scale bar, 20 μm.

measuring membrane tether forces using optically trapped beads [47], we found that fasudil treatment led to significantly higher membrane tension in SUM159 triple-negative breast cancer cells (Fig. 1a, b).

Irrespective of the specific pathway, endocytic processes rely on curvature generation at the plasma membrane, thus making them susceptible to inhibition by membrane tension [23, 48]. To assess the effects of fasudil on endocytosis, we focused on the dynamics of endocytic clathrin-coated carriers, as it was previously shown that the internalization of Fas is mediated by this pathway [49]. To this end, we used spinning-disk fluorescence microscopy to detect endocytic clathrin coats in live SUM159 cells that were genome-edited to express clathrin adaptor protein AP2 fused with GFP [50, 51]. Using the AP2 signal as a proxy for clathrin coats allowed us to decouple endocytic activity from the clathrin-mediated membrane trafficking originating from intracellular organelles [52]. As expected, the endocytic clathrin coats on the adherent surface of SUM159 cells became increasingly static after fasudil treatment (Fig. 1c). To quantitatively assess the changes in endocytosis dynamics, we measured the standard deviation (SD) of the clathrin coat growth rates [43], a robust indicator of clathrin-mediated endocytosis dynamics [28, 29], and observed a significant reduction following fasudil treatment (Fig. 1d). Contrary to fasudil treatment, increased actomyosin contractility by 30 nM leptin treatment for 24 h resulted in significant reduction in membrane tension and, consequently, increased endocytosis dynamics (Supplementary Fig. 1c–f). Overall, our results demonstrate an inverse relationship between membrane tension and actomyosin contractility, and that fasudil treatment results in increased membrane tension and impeded endocytosis dynamics.

Inhibition of endocytosis increases formation of Fas microaggregates on the cell surface

Given the ability of fasudil to slow endocytosis in cancer cells, we next aimed to investigate the effects of fasudil-mediated endocytosis inhibition on the membrane density and distribution of Fas receptors in a broad range of cancer cells. To accomplish this, Fas distribution in glioblastoma (U87), lung carcinoma (A549), liver carcinoma (HepG2), prostate cancer (PC3), and triple-negative breast cancer (SUM159) cells and in noncancerous human umbilical vein endothelial cells (HUVECs) was evaluated by immunofluorescence imaging. The Fas immunofluorescence signal was significantly higher in cancer cells than in HUVECs, in accordance with the previous studies reporting high levels of Fas expression in cancer cells [7–14] (Fig. 2a). Fas receptors were observed as bright punctae on the surface of the cancer cells, indicating microaggregate formation (Fig. 2a; Supplementary Video 1). As the next step, we sought to examine the effect of fasudil-mediated inhibition of endocytosis by treating these cells with 40 μM fasudil for 2 h. Upon treatment, the signal density of Fas microaggregates increased ~2-fold on cancer cells, whereas no effect was observed on HUVECs (Fig. 2a–c). These results demonstrate that inhibition of endocytosis by fasudil treatment enhances the formation of Fas microaggregates on the surface of cancer cells.

To corroborate the effects of endocytosis inhibition on Fas receptor density, we evaluated the formation of Fas microaggregates in cells treated with blebbistatin or dyngo-4a, which impede endocytosis dynamics mechanically and chemically, respectively. The myosin II inhibitor blebbistatin decreases actomyosin contractility in cells (Supplementary Fig. 1b), thereby

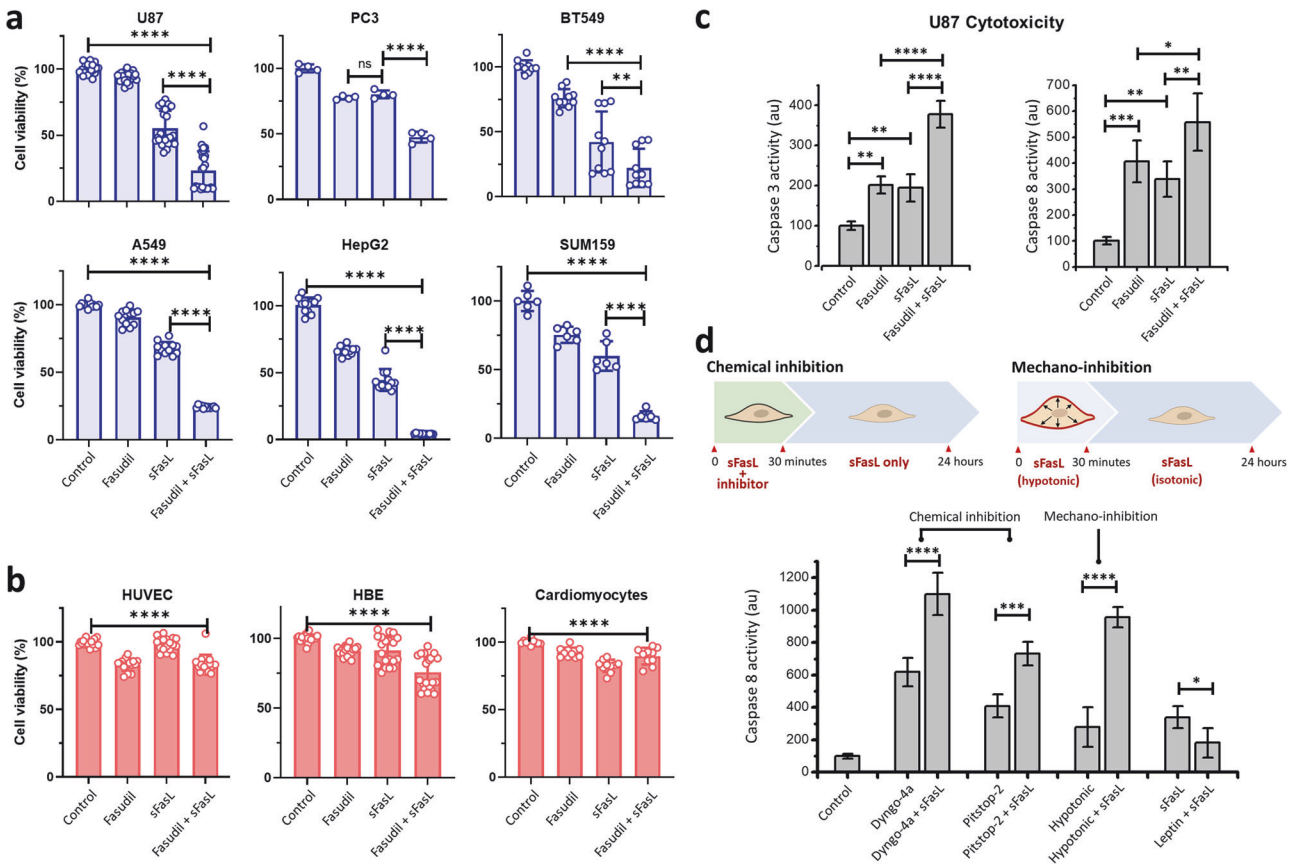

Fig. 3 Inhibition of endocytosis sensitizes cancer cells to sFasL. a Inhibition of endocytosis by 40 µM fasudil significantly decreased the viability of U87, PC3, BT549, A549, HepG2 and SUM159 cancer cells treated with 400 ng/mL sFasL. **b** The viability of HUVECs, HBEs, and iPS-cardiomyocytes significantly decreased upon the same treatment, but this decrease was not as dramatic as that observed in cancer cells. **c** Caspase-3 and caspase-8 activity in U87 cells significantly increased upon a combination of sFasL treatment with fasudil. **d** Schematics describe the experiments where inhibition of endocytosis was limited to 30 min and caspase-8 activity was quantified after 24 h (upper panel). Chemical inhibition was attained by treating cells with either 5 µM dyngo-4a or 2 µM pitstop-2. Mechano-inhibition involved increasing the plasma membrane tension of cells via hypotonic swelling for 30 min in the presence of sFasL. After this point, the hypotonic medium was replaced with isotonic medium (containing sFasL) to cease mechano-inhibition of endocytosis (****$p < 0.0001$, ***$p < 0.001$, **$p < 0.01$; *$p < 0.05$; one-way ANOVA).

increasing plasma membrane tension similar to fasudil [44, 53], whereas dyngo-4a inhibits receptor endocytosis by directly targeting the dynamin GTPase required for endocytic vesicle scission [54]. Consistent with the effects of fasudil, endocytosis inhibition by 10 µM blebbistatin or 5 µM dyngo-4a markedly increased the signal of Fas microaggregates on cancer cells treated for 2 h, whereas no such increase was observed in HUVECs (Fig. 2d, e).

We next aimed to elucidate the mechanism behind the increase in signal density of Fas microaggregates upon endocytosis inhibition. Using flow cytometry to quantify protein expression, we found that 40 µM fasudil treatment for 2 h results in no significant difference in the total expression levels of Fas (Supplementary Fig. 2a). To determine whether the increase in Fas signal density is exclusive to the cell surface, we used cold block to impede endocytosis and conducted immunofluorescence labeling without permeabilizing the plasma membrane. As expected, we found that fasudil treatment increases the surface expression of Fas in cancer cells (Supplementary Fig. 2b). As an alternative method, we used spinning disk confocal imaging to specifically analyze the ventral/adherent surface of the plasma membrane (Supplementary Fig. 2c). The fasudil- or dyngo-4a-mediated inhibition of endocytosis had no marked effect on the spatial density of Fas microaggregates on the adherent surface (Supplementary Fig. 2d). However, the mean immunofluorescence intensity of Fas microaggregates increased by up to one order of magnitude on the cancer cell surface but did not increase on the surface of noncancerous cells, i.e., HUVECs or human bronchial epithelial (HBE) cells (Supplementary Fig. 2e). Taken together, these results show that the inhibition of endocytosis does not affect the expression levels of Fas but promotes the growth of Fas microaggregates by increasing the number of Fas molecules on the cell surface.

Inhibition of endocytosis sensitizes cancer cells to soluble Fas ligand

Given that the modulation of endocytosis increases Fas localization at the cell surface, we next sought to evaluate whether inhibiting endocytosis sensitizes cancer cells to exogenous FasL treatment. To this end, we assessed cell viability by quantifying ATP levels in culture medium after 48 h of treatment with human recombinant sFasL alone or in combination with endocytosis inhibition. As shown in Fig. 3a, treatment with 400 ng/mL sFasL alone resulted in mild to moderate reduction in cancer cell viability (55.6%, 80.2%, 42.3%, 67.8%, 44.6%, and 59.9% in U87, PC3, BT549, A549, HepG2, and SUM159 cells, respectively, compared to the control). However, the addition of 40 µM fasudil increased the effect of sFasL, substantially decreasing the viability of the cancer cells (3.6–24.2%). As expected, unlike the effects observed in cancer cells, the viability of HUVECs, HBE cells, and

induced pluripotent stem cell (iPS)-derived cardiomyocytes was minimally affected by the combination of fasudil and sFasL (84.0%, 75.9%, and 89.6%, respectively, compared to the control) (Fig. 3b; Supplementary Videos 2, 3). Together, these results demonstrate that targeting endocytosis specifically increases the sensitivity of cancer cells to sFasL while sparing noncancerous cells.

To confirm that the reduction in viability is due to an increase in apoptosis, we monitored the activity of apoptotic markers caspase-3 and caspase-8 in U87 cells as we aimed to use these cells in our organoid and xenograft mouse models. In support of our hypothesis, we found that the inhibition of endocytosis upon fasudil treatment increased caspase-3 and caspase-8 activity in the presence of sFasL (Fig. 3c). To further corroborate that sensitization of U87 cells to sFasL is due to endocytosis inhibition, we performed cytotoxicity assays using alternative chemical and mechanical approaches to temporarily reduce endocytic rates. In our first approach, cells were pretreated with a combination of 400 ng/mL sFasL and a chemical endocytosis inhibitor (either 5 μM dyngo-4a or 2 μM pitstop-2) for 30 min and subsequently treated with 400 ng/mL sFasL only. After 24 h, we found that even transient inhibition of endocytosis dynamics (for 30 min) significantly increased caspase-8 activity in the presence of sFasL (Fig. 3d). In our second approach, we relied on a purely mechanical strategy to slow endocytosis dynamics. Specifically, we temporarily increased membrane tension by incubating U87 cells with 400 ng/mL sFasL in 80% hypotonic culture medium for 30 min, as hypo-osmotic swelling during this period is known to result in increased membrane tension and slower endocytosis dynamics [28, 30, 55]. After 30 min, the mechano-inhibition of endocytosis was ceased by replacing the medium with isotonic medium (100% culture medium) containing 400 ng/mL sFasL. Quantification of caspase-8 activity after 24 h revealed that a short exposure to hypotonic medium significantly increased the sensitivity of cancer cells to exogenous sFasL (Fig. 3d). On the contrary, caspase-8 activity in the presence sFasL reduced significantly when endocytosis dynamics are increased by 30 nM leptin treatment (Fig. 3d). To conclude, our findings demonstrate that inhibition of endocytosis increases the apoptotic efficacy of sFasL in cancer cells.

Fas-mediated apoptosis targets glioblastoma in a brain organoid model

Next, we wanted to assess the potential utility of sensitizing cancer cells to Fas-induced apoptosis as a strategy for targeted cancer therapy by testing in physiologically relevant contexts. Therefore, we generated a 3D in vitro glioblastoma model based on embryonic stem cell-derived cortical brain organoids [56] containing U87 glioblastoma cells labeled with red fluorescent protein (RFP). This approach allowed us to visualize and quantitatively assess changes in the glioblastoma mass within each organoid (Fig. 4a). Treatment with the combination of fasudil and sFasL (fasudil+sFasL) did not increase the percentage of apoptotic cells in 78-day-old brain organoids without U87 cells (Supplementary Fig. 3a, b). However, U87 cell-containing brain organoids treated with fasudil+sFasL for three days showed a dramatic decrease in the volume occupied by RFP-labeled U87 cells, leaving an acellular space (Fig. 4b, c). The organoids stained positively for the neural progenitor marker SOX2 and the differentiated neural marker anti-β-Tubulin III (TUJ1) before and after the treatment (Fig. 4b; Supplementary Fig. 3c). Altogether, these results demonstrate that treatment with fasudil+sFasL specifically increases Fas-induced apoptosis in glioblastoma cells in brain organoids and has a minimal effect on the viability of neural progenitor cells.

To assess the effect of fasudil+sFasL on U87 glioblastoma cells in brain organoids at single-cell resolution, we performed single-cell transcriptome analysis with a total of 1391, 1097, and 2149 cells derived from organoids that were untreated, treated for 24 h, or treated for 72 h, respectively. We identified 21 clusters that were systematically classified into 13 cell types, including neurons, astrocytes, neural progenitor cells, and glioblastoma cells (Fig. 4d, e). Uniform manifold approximation and projection (UMAP) plots showed a dramatic decrease in the number of glioblastoma cells after 24 h of treatment, with this population becoming negligible after 72 h of treatment (Fig. 4f, g). A comparison of the global transcriptomes of untreated organoids and those treated with fasudil+sFasL identified 611 and 252 genes that were significantly up- and downregulated by treatment, respectively. Gene Ontology analysis revealed that the upregulated genes are enriched in the oxidative stress response (e.g., *GCLM*, *HSF1*, and *OGG1*), apoptosis (e.g., *MSH6*, *DNAJA1*, and *TRAP1*) and DNA repair (e.g., *FOXO4*, *MDM4*, and *CUL4A*) (false discovery rate (FDR) < 0.05 by hypergeometric test). In contrast, the glycoprotein (e.g., *MVD* and *OST4*), ATP (e.g., *COX5B* and *COX6C*), sterol (e.g., *NPC1* and *NPC2*) and collagen metabolic processes (e.g., *MMP2* and *VIM*) were significantly downregulated (FDR < 0.05) (Fig. 4h). The upregulation of cell death-related genes and downregulation of metabolic genes in response to fasudil+sFasL were more pronounced in glioblastoma cells than in noncancer cells, such as neurons, and neural progenitor cells. Interestingly, both apoptotic and metabolic genes were upregulated in astrocytes after treatment (Fig. 4h).

Combination therapy of U87 glioblastoma in vivo xenografted tumors with fasudil and sFasL

Motivated by the targeted killing of U87 glioblastoma cells within cortical organoids, we further evaluated the antitumor efficacy of fasudil and sFasL as monotherapy and in combination using a subcutaneous U87 cell xenograft tumor model in athymic nude mice. In our preliminary in vivo assays, we found that, although high doses of sFasL result in systemic toxicity, the combination of 50 mg/kg Fasudil + 180 μg/kg sFasL is tolerated by mice upon intraperitoneal delivery (see Supplementary Fig. 4). However, this treatment led to no significant difference in tumor growth between the treatment arms (i.e., sFasL monotherapy, fasudil monotherapy and fasudil+sFasL) and the vehicle arm (Supplementary Fig. 4). Next, in an attempt to increase local drug concentration, the drugs were administered intratumorally twice a week in the beginning of the assay and the treatment route was switched to intraperitoneal administration after two weeks. We found that, 26 days after tumor cell implantation, the combination treatment (i.e., fasudil+sFasL) significantly inhibited tumor growth compared to vehicle or monotherapy (Fig. 5a). The median survival of mice treated with vehicle, fasudil or sFasL monotherapy ranged from 27–28 days, with fewer than 40% of the animals surviving one month after tumor cell implantation (Fig. 5b). Whereas, 26 days post implantation, while 37.5% (3/8) of mice in the control group reached endpoint, none of the mice in the combination treatment arm reached endpoint and tumor growth was observed in only one mouse. Fifty percent (4/8) of the mice in the combination arm showed tumor regression, and notably, one of the mice showed complete tumor regression (Fig. 5c). These results demonstrate that the local administration of fasudil+sFasL, but not either alone, significantly suppresses glioblastoma tumor growth, with potential curative effects in vivo. Overall, our results in cortical organoids and mouse xenograft tumor models demonstrate that sFasL can potentially be utilized as an effective and selective anticancer drug when combined with fasudil-mediated endocytosis inhibition.

DISCUSSION

Dysregulation of endocytosis has been linked to pathogenesis of numerous diseases [57–59]. Endocytosis dynamics are elevated in cancer cells to help reduce the expression of membrane proteins [57, 60, 61], including death receptors [59, 62]. Herein, we

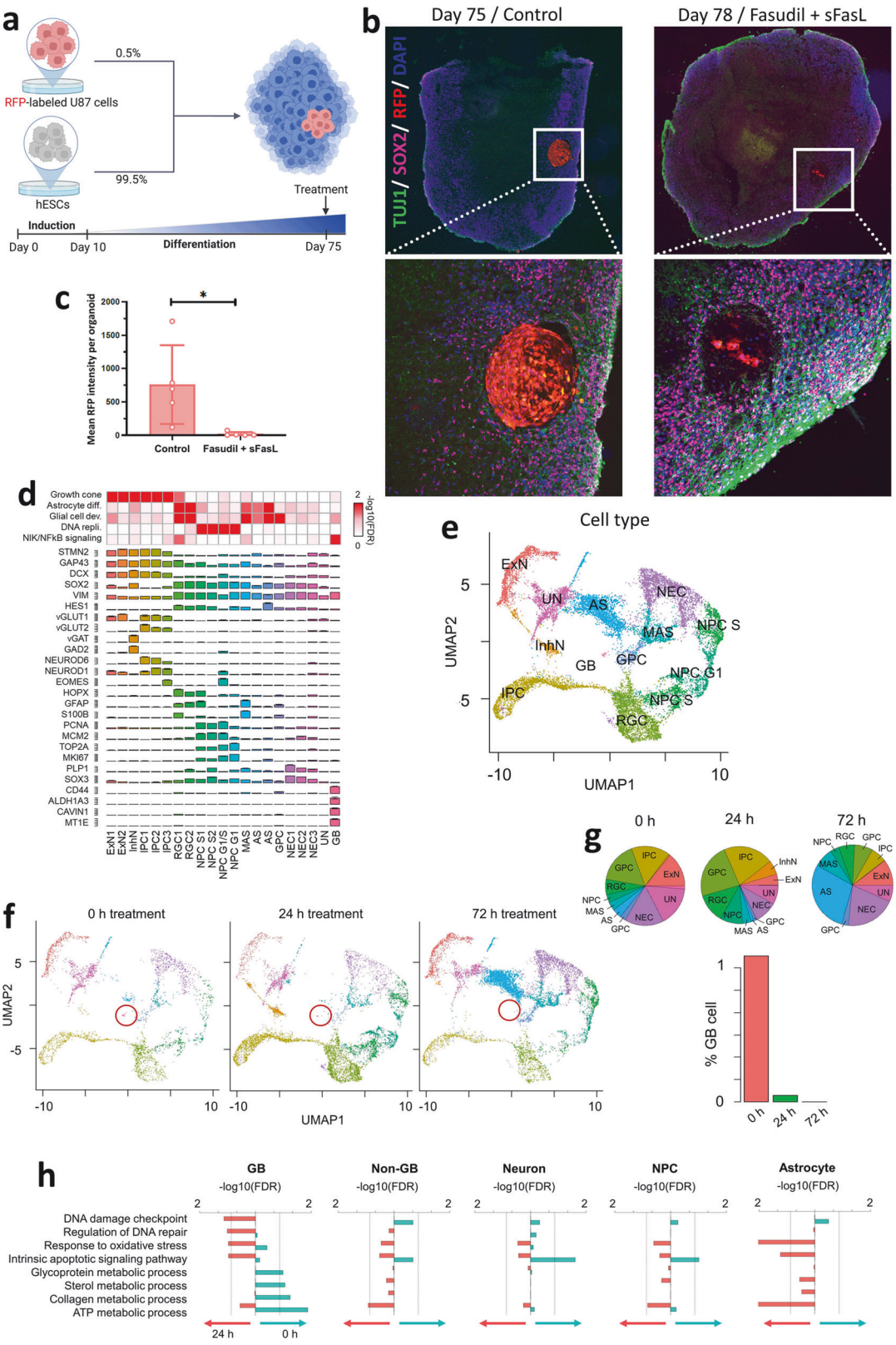

demonstrate that fasudil, a clinically utilized vasodilator, increases mechanical tension on the plasma membrane and impedes endocytosis dynamics in cancer cells. Our results suggest that the increase in membrane tension is due to increased membrane-cytoskeleton adhesion upon reduced acto-myosin contractility, as proposed earlier [44]. Mechano-inhibition of endocytosis will enable further dissection of endocytosis function at the systemic level in different disease states, including cancer.

Cancer cells co-opt mechanisms to exploit Fas expression as a survival factor while circumventing Fas-induced apoptosis [15].

Fig. 4 Fas-mediated apoptosis targets glioblastoma in a brain organoid model. a Cortical brain organoids were formed by culturing human embryonic stem cells (hESCs, 99.5%) with red fluorescent protein (RFP)-expressing U87 glioblastoma cells (0.5%). **b**–**c** Seventy-five-day-old organoids were imaged using spinning disk fluorescence microscopy, where the glioblastoma mass could be distinguished using RFP signal. Upon treatment with fasudil+sFasL, the RFP-expressing regions had almost disappeared by day 78 ($p = 0.022$; unpaired t test). **d**–**e** Cell types in the u*niform manifold approximation and projection* (UMAP) plot of glioblastoma brain organoids. ExN: excitatory neurons, InhN: inhibitory neurons, IPC: intermediate progenitor cells, RGC: radial glia cells, NPC: neural progenitor cells, MAS: mature astrocytes, AS: astrocytes, GPC: glial progenitor cells, NEC: neuroepithelial cells, UN: unknown cell type, and GB: glioblastoma cells. **f** UMAP plots of glioblastoma brain organoids after 0, 24, and 72 h of treatment with fasudil+sFasL. The glioblastoma cluster (circled in red) shrank and eventually disappeared. **g** Percentages of varying cell types in the organoid at the three different time points. The percentage of GB cells approached zero after 72 h of treatment. **h** After 24 h of fasudil+sFasL treatment, the expression of genes related to apoptotic pathways, DNA damage, and oxidative stress increased in GB cells, but that of genes related to metabolic processes decreased.

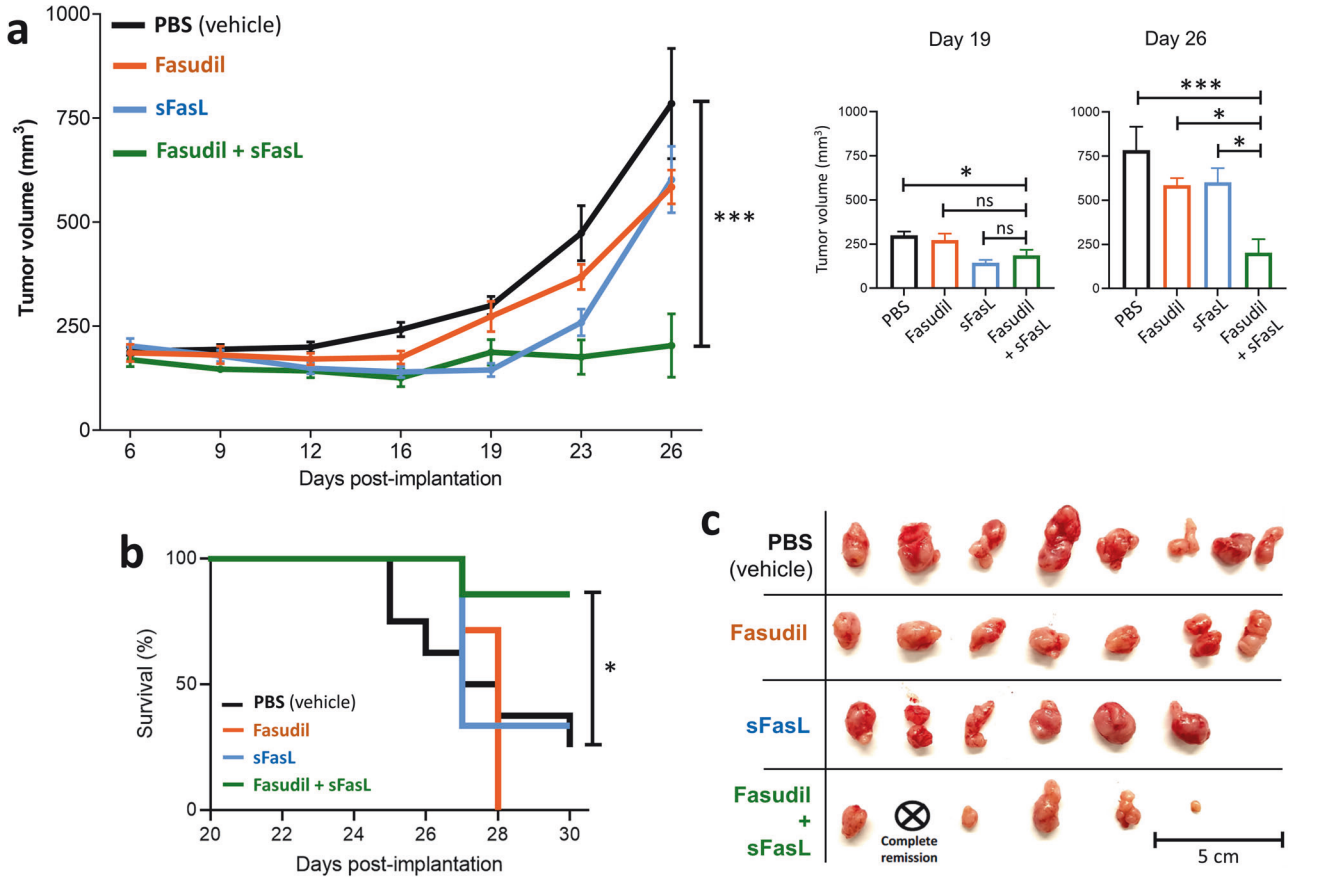

Fig. 5 Local administration of fasudil and sFasL suppresses U87 glioblastoma growth in vivo. a Tumor sizes in fasudil+sFasL treatment arm was significantly smaller than those in any other group at the end of the treatment. Panels on the right show the tumor sizes (mean ± sd) measured on 19- and 26-days post-implantation (***$p < 0.001$, **$p < 0.01$, and *$p < 0.05$; ordinary one-way ANOVA). **b** The survival probability in the fasudil+sFasL group was significantly higher than that in any other group [log-rank (Mantel–Cox) test; compared to the combination group: PBS $p = 0.022$, fasudil $p = 0.006$, and sFasL $p = 0.048$]. **c** Extracted tumors one month after implantation. The tumor in one of the mice in the fasudil+sFasL combination group was completely eliminated.

Our study aimed to sensitize cancer cells to Fas-induced apoptosis to transform this cell survival strategy into targeted cancer therapy. We show that inhibition of endocytosis promotes the formation of Fas microaggregates on the cell surface and thus decreases the ability of cancer cells to resist Fas-induced apoptosis. In a physiological context, this sensitivity can be activated via mechano-inhibition of endocytosis by fasudil. Overall, our results in cortical organoids and a mouse xenograft tumor model demonstrate that sFasL combined with fasudil has potential utility as an effective and selective anticancer therapeutic regimen.

Our results demonstrate that endocytosis inhibition does not affect the expression of Fas but increases the surface availability, promoting Fas microaggregation on the cancer cell surface. So far, there have been opposing reports regarding whether internalization of TNF family receptors form the cell surface is required for the induction of death receptor-induced apoptosis [49, 63, 64]. Our findings support models proposing that the internalization of the death receptors from the plasma membrane is not required for activation of the caspase cascade [64, 65].

We note that the cytotoxic activity of sFasL is orders of magnitude lower than that of membrane delivered FasL [8]. It was previously proposed that tumor cells release sFasL as a means to antagonize the effects of membrane-bound FasL [8, 66] or evade immune response [67]. Further investigations may establish whether sFasL shed by cancer cells may account for the increased

caspase-8 activity observed in our assays upon endocytosis inhibition (mechanical or chemical) even in the absence of exogenous sFasL.

Finally, emerging research shows that cancer cells exhibit significantly lower membrane tension compared to their non-malignant counterparts [36–38]. Future investigations may delve into whether this reduced plasma membrane tension renders cancer cells more susceptible to mechano-inhibition of endocytosis. Moreover, exploring the mechanical characteristics of cancer cells could unveil opportunities to enhance the specificity of targeted therapies. This line of inquiry holds promise for advancing our understanding of cancer biology and optimizing therapeutic strategies.

MATERIALS AND METHODS

hESCs culture

BC4 hESCs [56] were cultured on Matrigel (BD Biosciences) coated dishes with mTeSR1 media (Stem Cell Technologies) and passaged every week by disassociating with 0.83 U/mL Dispase (Stem Cell Technologies). All experiments including hESCs were approved by Yale Embryonic Stem Cell Research Oversight (ESCRO).

Cancer cell culture

U87, A549, and HepG2 cell lines were purchased from ATCC and were cultured in DMEM supplemented with 10% FBS and 1% pen/strep (Thermo Fischer). PC3 and BT549 cells were donated by Yale Center for Precision Cancer Modeling (YCPCM) and cultured in F-12 (Thermo Fischer) or RPMI (Thermo Fischer) media supplemented with 10% FBS and 1% pen/strep, respectively. SUM159 cells genome edited to express AP2-EGFP were donated by Tomas Kirchhausen's group at Harvard Medical School [51]. SUM159 cells were cultured in F-12 media supplemented with 5% FBS, 1% pen/strep, 1 mg/ml hydrocortisone (Sigma Aldrich) and 10 mg/ml insulin (Sigma Aldrich). Cells were kept at optimal density by passaging when needed. In viability experiments, cells were treated with different combinations of 400 ng/mL human recombinant sFasL (Biolegend), 40 µM Fasudil HCl (SellekChem), 10 µM Blebbistatin (Sigma), 5 µM Dyngo-4a (Cayman Chemical), or 2 µM Pitstop-2 (Abcam), hypotonic medium (80% of medium was replaced with water) in 96-well plates for 48 h. Cell viability was quantified by detection of ATP content in the culture medium with CellTiter-Glo® Luminescent Cell Viability Assay (Promega) by following the manufacturer's instructions. To assess the rate of apoptosis, caspase-3 and caspase-8 activities were measured using the EnzChek Caspase-3 Activity Assay Kit and the CaspGLOW™ Fluorescein Active Caspase-8 Staining Kit, respectively. The fluorescence generated by active caspase-3 and −8 formation was monitored at 25 °C at excitation wavelengths ($\lambda_{ex} = 485$ nm) and emission wavelengths ($\lambda_{em} = 535$ nm) using an Infinite M1000 Pro plate reader (Tecan, Baldwin Park, CA, USA). Leptin (Sigma) concentration used in the caspase assays was 30 nM.

Immunofluorescence microscopy and image analysis

Cells were fixed with ice cold 3.7% paraformaldehyde (Sigma-Aldrich), permeabilized with 0.1% Triton X-100 (Fisher Biotech, Hampton, NH, USA), and blocked with PBS supplemented with goat serum (2%, v/v) (Southern biotech) and 0.1% Tween-20 (Thermo Fisher). Cells were then incubated with FAS Mouse anti-Human (Clone: 4F8H6, Invitrogen) at 1:500 dilution and the appropriate fluorochrome-conjugated secondary antibody (Alexa Fluor 647 anti-mouse IgG1, Fischer Scientific) for Fas immunostaining. For labeling of actin filaments and pERM, cells were treated with Phalloidin AF405 (Thermo Fischer Scientific, 1:2000 dilution) and anti-pERM (Cell Signaling Technology #3726, 1:500) for 10–15 min at room temperature, following either the blocking step or secondary antibody labeling, depending on the experimental design. For nuclei staining, cells were incubated with Hoechst (1:2000) for 2 min at room temperature after secondary antibody labeling.

To assess surface-associated Fas expression, cells were maintained at 4 °C (or on ice) throughout the procedure and all reagents were kept ice-cold to prevent antibody internalization post-treatment. Following treatment, cells were washed twice with PBS and subsequently incubated with Fas Mouse anti-Human antibody (clone DX2, BD Biosciences) at a 1:100 dilution at 4 °C. Next, cells were treated with the appropriate fluorochrome-conjugated secondary antibody, Alexa Fluor 568 anti-mouse IgG1 (Fisher Scientific), for 40 min at 4 °C with 1:2000 dilution. Finally, cells were fixed with ice-cold 3.7% PFA (Sigma-Aldrich) and imaged.

For quantitative analysis of cell surface-associated Fas expression, fluorescent images of the immunostained cells were collected using a Nikon TIE fluorescence microscope equipped with a CSU-W1 spinning disk unit (Yokogawa Electric Corporation), 100× objective lens (Nikon CFI Plan-Apochromat Lambda, NA 1.45), sCMOS camera (Prime 95B; Teledyne Photometrics), and 488- and 640-nm excitation lasers with 100 mW of nominal power. Images were acquired at a rate of 0.25–0.5 Hz with a laser exposure of 100 ms per frame. Image acquisition was performed using NIS Elements software.

A comparative analysis of Fas expression was conducted using Fiji software (https://imagej.net/Fiji/Downloads) by quantifying signal intensities obtained from confocal sections. To quantify the number, size, and area fraction of Fas puncta, the surface area of each cell was demarcated and subsequently masked to create binary images by using the 'analyze particles' function of the same software [68]. After background subtraction, original image sections were multiplied by the mask obtained from the same field of view. For each cell, the mean intensity of spots was calculated by dividing the integrated intensity of the selected area by the number of detected spots.

Actin rearrangement and the cellular distribution of pERM were assessed through quantification of actin and pERM signal intensities in the peripheral regions, defined as the outermost 20% of the whole cell diameter, against central regions, encompassing 60% of the cell diameter.

Membrane tether force measurements

Membrane tether force measurements were conducted at 37° C using the C-Trap optical tweezers system (LUMICKS, Amsterdam, The Netherlands). SUM159 cells gene-edited to express AP2–eGFP [51] were plated in a custom-designed flow chamber 15–24 h prior to the experiments and incubated at 37°C and 5% CO_2. The flow chamber was composed of a microscope cover glass (No 1.5, Fisher Scientific), a layer of parafilm tape as a separator, and a 1.0 mm thick microscope slide (Fisher Scientific). This selection of thicknesses for the cover glass, parafilm, and glass slide is designed for the flow channel to be compatible with the working distance of our C-Trap objective and condenser.

Tethers were pulled from the plasma membrane using streptavidin-coated polystyrene beads with a mean diameter of 1.87 µm (SVP-15, Spherotech). Right before the experiments, F-12 growth medium was replaced with phenol red-free L15 imaging medium (Thermo Fisher Scientific) supplemented with 10% FBS (containing the beads) and the flow channel inlet and outlet were immediately sealed. The imaging medium was prepared by diluting the bead suspension down to 0.01% w/v, spinning and resuspending the suspension once in PBS and then in phenol red-free L15 medium supplemented with 10% FBS.

The trap stiffness was calibrated using the thermal noise spectrum. After calibration, the trap stage was moved at a speed of 1 µm/s until the bead contacted the cell. After 4–10 s, the stage was moved in the opposite direction at a speed of 5µm/s to attain a tether length of 10µm. The tether was then held stationary for up to a minute to measure the static tether force as described previously [47].

Imaging clathrin-mediated endocytosis dynamics in live cells

Fluorescence imaging was performed using a Nikon TIE fluorescence microscope equipped with a CSU-W1 spinning disk unit (Yokogawa Electric Corporation), a 100× objective lens (Nikon CFI Plan-Apochromat Lambda, NA 1.45), a sCMOS camera (Prime 95B; Teledyne Photometrics), and 488 nm excitation lasers with 100 mW of nominal power and temperature-controlled chamber. NIS Elements image acquisition software was used for acquisition of 2D time-lapse movies.

Endocytic clathrin dynamics were captured in SUM159 cells genome edited to express AP2-EGFP [51]. 15–24 h prior to imaging, cells were plated on a glass bottom dish (MatTek Life Sciences) and incubated at 37 °C with 5% CO_2. Cells were imaged in phenol red-free L15 medium (Thermo Fisher Scientific) supplemented with 10% FBS and 5% (v/v) penicillin/streptomycin at a rate of 0.25 Hz with laser exposure of 100 ms per frame. Two-dimensional time-lapse movies were acquired using NIS Elements software.

Individual clathrin-coated structures were captured and endocytic events were detected using TraCKer and cmeAnalysis softwares [43, 52, 69]. Clathrin coat growth rate analysis was conducted was previously described [43] to assess the changes in clathrin-mediated endocytosis dynamics.

Glioblastoma model in cortical brain organoids

As described previously [56], hESCs were dissociated into single cells via Accutase and 9000 cells, containing 0.5% RFP-infected U87 cells were plated into a well of U-bottom ultra-low-attachment 96-well plates. Neural induction medium (DMEM-F12, 15% (v/v) KSR, 5% (v/v) heat-inactivated FBS (Life Technologies), 1% (v/v) Glutamax, 1% (v/v) MEM-NEAA, 100 µM β-mercaptoethanol, 10 µM SB-431542, 100 nM LDN-193189, 2 µM XAV-939 and 50 µM Y27632) was used as culture media for ten days. Organoids were transferred to ultra-low-attachment six-well plate in hCO media without vitamin A (1:1 mixture of DMEM-F12 and Neurobasal media, 0.5% (v/v) N2 supplement, 1% (v/v) B27 supplement without vitamin A, 0.5% (v/v) MEM-NEAA, 1% (v/v) Glutamax, 50 µM β-mercaptoethanol, 1% (v/v) penicillin/streptomycin and 0.025% insulin) at day ten and the media was changed every other day. At day 18, Vitamin A, brain-derived neurotrophic factor, and ascorbic acid were added to the culture medium. Organoids with or without glioblastoma were treated with sFasL+fasudil combination after Day 75 for 72 h for viability studies.

Immunofluorescence microscopy and image analysis for organoids

Organoids were fixed in 3.7% paraformaldehyde at 4 °C overnight followed by three washes with PBS at room temperature. Then, organoids were incubated in a 30% sucrose solution for 2 days at 4 °C. Organoids were equilibrated with an optical cutting temperature compound at room temperature for 15 min, transferred to base molds, and embedded in an optical cutting temperature compound on dry ice. Then, 40-µm cryosections were generated, and organoid blocks were stored at −80 °C. Slides were dried for 2 h at room temperature and incubated with 0.1% Triton-100 for 15 min at RT in a humidified chamber. Organoids were blocked with 3% BSA at room temperature for 2 h, and then were incubated with the primary antibodies (mouse anti-Sox-2 and rabbit anti-TUJ-1) diluted 1:100 in 3% BSA overnight at 4 °C. After two washing steps, organoids were incubated with Alexa Fluor Dyes (1:500) for 1 h following nuclei staining with DAPI (1:1,000). Finally, slides were mounted with ProLong Gold Antifade Reagent and images were taken with a CSU-W1 spinning disk unit (Yokogawa Electric Corporation), 20× objective lens (CFI Plan Apochromat Lambda 20x/0.75, WD 1 mm, No: MRD00205), Andor iXon camera (Ultra888 EMCCD, 1024 × 1024 (pix), 13 um pixel), and 488-, 550-, and 640-nm excitation lasers with 100 mW of nominal power. DNA strand breaks were detected with TUNEL stain (11684795910, Sigma) to detect apoptotic or dead cells following the manufacturer's protocol. The ratio of the mean signal intensity for TUNEL stain to DAPI was calculated for each image.

For quantitative analysis of TUJ1 and SOX2 staining in the organoids, manual masks of the maximum intensity projection of the images were generated using ImageJ. The DAPI signal in these masks was used to segment the nuclei and postprocess the data using the Python package scikit-image. Nuclei segmentation was performed using Cellpose, with a user-trained model. The masks retrieved by Cellpose were then expanded by three pixels radially using the function expand_labels (from sci-kit image) to encapsulate the entire cell. For each of the cell masks, the mean intensity in the TUJ1, SOX2 and DAPI channels was calculated using the function skimage.measure.regionprops and the background intensity was subtracted.

Flow cytometry analysis

Cells were cultured under specified conditions, then washed with Phosphate-Buffered Saline (PBS) and detached using trypsin in preparation for counting and staining procedures. To evaluate Fas (CD95) expression, 3.0×10^5 cells were suspended in 3.7% Paraformaldehyde (PFA) and incubated for 15 min at 4 °C in the dark. This was followed by a permeabilization step with 0.1% Triton X-100 for 20 min at 4 °C in the dark. After each step, cells were washed with PBS to remove any residual reagents. For blocking, cells were treated with 3% Bovine Serum Albumin (BSA) in Flow Cytometry Staining buffer (Thermo Fisher) overnight (ON). Subsequently, cells were stained with either CD95 APC antibody (Clone 1507, Thermo Fisher) or the APC IgG1 antibody (Thermo Fisher) as an isotype control. The staining was performed for 45 min at 4 °C in the dark. Following staining, cells were washed twice with PBS and kept on ice prior to flow cytometry analysis.

The stained cells were analyzed using a Becton Dickinson LSR II flow cytometer at the Ohio State University Flow Cytometry Shared Resources. Data analysis was conducted using FlowJo software (version 8.8.6, Treestar Inc). Initial gating with FSC-A and SSC-A was performed to exclude dead cells, and subsequently, FSC-W and SSC-W gating was employed to eliminate doublets. For each sample, ~10,000 events were captured, and the mean fluorescence intensity of the CD95 APC was analyzed using FlowJo software.

Data processing of single-cell RNA-seq

Single-cell RNA-seq reads were mapped to GRCh38 human genome (GRCh38–2020-A) and counted with Ensembl genes using the count function of CellRanger software (v3.0.2) with default parameters. Batch effect and intrinsic technical effects were normalized by Seurat (v3.0.2) [70]. Briefly, we filtered out cells with less than 50 detected genes and more than 15% of mitochondria-derived reads as low-quality samples. Raw UMI count was normalized to total UMI count in each library. Top 2,000 highly variable genes were used to identify cell pairs anchoring different scRNA-seq libraries using 20 dimensions of canonical correlation analysis. All scRNA-seq libraires used in this study were integrated into a shared space using the anchor cells. After scaling gene expression values across all integrated cells, we performed dimensional reduction using principal component analysis (PCA). For the visualization, we further projected single cells into two-dimensional UMAP space from the 1st and 20th PCs. Graph-based clustering was then implemented with shared nearest neighbor method from the 1st and 20th PCs and 0.8 resolution value. Differentially expressed genes (DEGs) in each cluster were identified with more than 1.25-fold change and $p < 0.05$ by a two-sided unpaired T test. Gene Ontology analysis was performed to the DEGs by GOstats Bioconductor package (v2.46.0) [71]. The false discovery rate was adjusted by p.adjust function in R with "method = "BH"" parameter.

Cluster labeling was performed by unique markers, Gene Ontology, and enrichment of gene signatures as described previously [56, 72]. Briefly, neuronal and non-neuronal clusters were separated by neuronal growth cone (*STMN2*, *GAP43*, and *DCX*) and early neurogenesis markers (*VIM*, *SOX2* and *HES1*). Neuronal clusters are further classified into excitatory and inhibitory neurons by expression of glutamate (*vGLUT1/2*) and GABA transporters (*vGAT*), respectively. In addition, neurons expressing neuroblast markers (*NEUROD1/6*) were labeled as intermediate progenitor cells (IPCs), which are transitioning to newborn neurons [73]. Non-neuronal clusters are classified into mitotic and non-mitotic cells with the presence and absence of cell cycle-related gene expression, respectively. The mitotic clusters were labeled as NPC S, NPC S/G1, or NPC G1 by S (*PCNA*, *MCM2*) and G1 phase markers (*TOP2A*, and *MKI67*). The non-mitotic clusters with significant overrepresentation of a GO term "Astrocyte differentiation (GO:0048708)" were assigned to astrocytes. Astrocyte clusters with high expression of *GFAP* and *S100B* were further labeled as mature astrocytes. *HOPX*-expressing non-mitotic clusters were assigned to radial glia cells. A non-mitotic cluster without astrocyte marker expression, but with significant overrepresentation of "glial cell development (GO:0021782)" was labeled as a glial progenitor cell. Neuroepithelial cells were assigned by expression of its markers (*PLP1* and *SOX3*). Glioblastoma clusters were assigned by unique expression of GBM biomarkers (*CD44*, *ALDH1A3*, *CAVIN1*, and *MT1E*). Global comparison of transcriptome profiles was performed by 1.25-fold average expression difference and $p < 0.05$ of two-sided unpaired T test between 72h-treated and non-treated organoids.

Fasudil+sFasL combination therapy in U87 glioblastoma xenograft tumors

Ten million U87 glioblastoma cells (ATCC) were implanted subcutaneously into the right flank of immune-deficient athymic nude mice (Jackson Labs) in a 1:1 mix of plain growth media and Matrigel (Corning). After approximately one week post transplantation when the tumors were palpable, with tumor volumes ranging from 50–200 mm^3 7–8 tumor bearing mice were randomly assigned to the following four treatment arms: Vehicle (PBS), sFasL monotherapy, fasudil monotherapy and fasudil +sFasL combination. On Mondays and Thursdays, the Fasudil monotherapy and the fasudil+sFasL combination arms received a priming dose of 50 mg/kg Fasudil, while the sFasL only and PBS groups received an equivalent volume of PBS injection. Twenty-four hours after the priming injections, PBS, sFasL (180 µg/kg), fasudil (50 mg/kg) or fasudil (50 mg/kg) and sFasL (180 µg/kg) in combination, was administered to the relevant arms. Our maximum tolerated dose (MTD) studies demonstrated that the drug combinations used in this study do not cause fatality or significant weight loss in mice (Supplementary Fig. 4a).

In the first study, the route of administration was intra-peritoneal for the entire study. In the second study, the route of drug administration was intra-tumoral to the central tumor mass for two weeks but switched to intra-peritoneal due to observation of trauma and tissue dehiscence at the

injection sites. Tumor dimensions were recorded by caliper measurements at three-day intervals and volumes calculated using the formula: (length x width^2)/2. Treatment was ceased and the mice were euthanized after endpoint volume of 1000 mm^3 was reached in the vehicle arm. Tumors were excised from mice from all arms and images taken at the end of the study.

All in vivo experiments were carried out in accordance with the Yale University's Institutional Animal Care and Use Committee (IACUC protocol #20218-2021).

DATA AVAILABILITY

The data supporting the findings of this study are available from the corresponding author upon reasonable request.

REFERENCES

1. Nagata S. Fas Ligand-Induced Apoptosis. Annu Rev Genet. 1999;33:29–55.
2. Nagata S. Apoptosis by Death Factor. Cell. 1997;88:355–65.
3. Tanaka M, Suda T, Takahashi T, Nagata S. Expression of the functional soluble form of human Fas ligand in activated lymphocytes. EMBO J. 1995;14:1129–35.
4. Kischkel FC, Hellbardt S, Behrmann I, Germer M, Pawlita M, Krammer PH, et al. Cytotoxicity-dependent APO-1 (Fas/CD95)-associated proteins form a death-inducing signaling complex (DISC) with the receptor. EMBO J. 1995;14:5579–88.
5. Schütze S, Tchikov V, Schneider-Brachert W. Regulation of TNFR1 and CD95 signalling by receptor compartmentalization. Nat Rev Mol Cell Biol. 2008;9:655–62.
6. Sharma S, Carmona A, Skowronek A, Yu F, Collins MO, Naik S, et al. Apoptotic signalling targets the post-endocytic sorting machinery of the death receptor Fas/CD95. Nat Commun. 2019;10:3105.
7. Trauth BC, Klas C, Peters AMJ, Matzku S, Möller P, Falk W, et al. Monoclonal antibody-mediated tumor regression by induction of apoptosis. Science. 1989;245:301–5.
8. Schneider P, Holler N, Bodmer JL, Hahne M, Frei K, Fontana A, et al. Conversion of membrane-bound Fas(CD95) ligand to its soluble form is associated with downregulation of its proapoptotic activity and loss of liver toxicity. J Exp Med. 1998;187:1205–13.
9. Rensing-Ehl A, Frei K, Flury R, Matiba B, Mariani SM, Weller M, et al. Local Fas/APO-1 (CD95) ligand-mediated tumor cell killing in vivo. Eur J Immunol. 1995;25:2253–8.
10. O'Brien DI, Nally K, Kelly RG, O'Connor TM, Shanahan F, O'Connell J. Targeting the Fas/Fas ligand pathway in cancer. Expert Opin Ther Targets. 2005;9:1031–44.
11. Carneiro BA, El-Deiry WS. Targeting apoptosis in cancer therapy. Nat Rev Clin Oncol. 2020;17:395–417.
12. Ogasawara J, Watanabe-Fukunaga R, Adachi M, Matsuzawa A, Kasugai T, Kitamura Y, et al. Lethal effect of the anti-Fas antibody in mice. Nature. 1993;364:806–9.
13. Algeciras-Schimnich A, Pietras EM, Barnhart BC, Legembre P, Vijayan S, Holbeck SL, et al. Two CD95 tumor classes with different sensitivities to antitumor drugs. Proc Natl Acad Sci USA 2003;100:11445–50.
14. Peter ME, Legembre P, Barnhart BC. Does CD95 have tumor promoting activities? Biochim Biophys Acta - Rev Cancer. 2005;1755:25–36.
15. Peter ME, Hadji A, Murmann AE, Brockway S, Putzbach W, Pattanayak A, et al. The role of CD95 and CD95 ligand in cancer. Cell Death Differ. 2015;22:549–59.
16. Irmler M, Thome M, Hahne M, Schneider P, Hofmann K, Steiner V, et al. Inhibition of death receptor signals by cellular FLIP. Nat 1997 3886638. 1997;388:190–5.
17. Delmas D, Rébé C, Micheau O, Athias A, Gambert P, Grazide S, et al. Redistribution of CD95, DR4 and DR5 in rafts accounts for the synergistic toxicity of resveratrol and death receptor ligands in colon carcinoma cells. Oncogene. 2004;23:8979–86.
18. Muppidi JR, Siegel RM. Ligand-independent redistribution of Fas (CD95) into lipid rafts mediates clonotypic T cell death. Nat Immunol. 2004;5:182–9.
19. Ivanov VN, Bergami PL, Maulit G, Sato TA, Sassoon D, Ronai Z. FAP-1 Association with Fas (Apo-1) Inhibits Fas Expression on the Cell Surface. Mol Cell Biol. 2003;23:3623–35.
20. Ivanov VN, Ronai Z, Hei TK. Opposite roles of FAP-1 and dynamin in the regulation of Fas (CD95) translocation to the cell surface and susceptibility to Fas ligand-mediated apoptosis. J Biol Chem. 2006;281:1840–52.
21. Winterhoff BJN, Arlt A, Duttmann A, Ungefroren H, Schäfer H, Kalthoff H, et al. Characterisation of FAP-1 expression and CD95 mediated apoptosis in the A818-6 pancreatic adenocarcinoma differentiation system. Differentiation. 2012;83:148–57.
22. Bennett M, Macdonald K, Chan SW, Luzio JP, Simari R, Weissberg P. Cell Surface Trafficking of Fas: A Rapid Mechanism of p53-Mediated Apoptosis. Science. 1998;282:290–3.
23. Sheetz MP. Cell control by membrane-cytoskeleton adhesion. Nat Rev Mol Cell Biol. 2001;2:392–6.
24. Gauthier NC, Masters TA, Sheetz MP. Mechanical feedback between membrane tension and dynamics. Trends Cell Biol. 2012;22:527–35.
25. Masters TA, Pontes B, Viasnoff V, Li Y, Gauthier NC. Plasma membrane tension orchestrates membrane trafficking, cytoskeletal remodeling, and biochemical signaling during phagocytosis. Proc Natl Acad Sci USA 2013;110:11875–80.
26. Djakbarova U, Madraki Y, Chan ET, Kural C. Dynamic interplay between cell membrane tension and clathrin-mediated endocytosis. Biol Cell. 2021;0:1–30.
27. Boulant S, Kural C, Zeeh JC, Ubelmann F, Kirchhausen T. Actin dynamics counteract membrane tension during clathrin-mediated endocytosis. Nat Cell Biol. 2011;13:1124–31.
28. Ferguson JP, Huber SD, Willy NM, Aygün E, Goker S, Atabey T, et al. Mechanoregulation of clathrin-mediated endocytosis. J Cell Sci. 2017;130:3631–6.
29. Willy NM, Ferguson JP, Huber SD, Heidotting SP, Aygün E, Wurm SA, et al. Membrane mechanics govern spatiotemporal heterogeneity of endocytic clathrin coat dynamics. Mol Biol Cell. 2017;28:3480–8.
30. Willy NM, Colombo F, Huber S, Smith AC, Norton EG, Kural C, et al. CALM supports clathrin-coated vesicle completion upon membrane tension increase. Proc Natl Acad Sci. 2021;118:e2010438118.
31. Pouille PA, Ahmadi P, Brunet AC, Farge E. Mechanical signals trigger Myosin II redistribution and mesoderm invagination in Drosophila embryos. Sci Signal. 2009;2:ra16.
32. Tobys D, Kowalski LM, Cziudaj E, Müller S, Zentis P, Pach E, et al. Inhibition of clathrin-mediated endocytosis by knockdown of AP-2 leads to alterations in the plasma membrane proteome. Traffic. 2021;22:6–22.
33. Bergert M, Lembo S, Sharma S, Russo L, Milovanović D, Gretarsson KH, et al. Cell Surface Mechanics Gate Embryonic Stem Cell Differentiation. Cell Stem Cell. 2021;28:209–16.e4.
34. De Belly H, Stubb A, Yanagida A, Labouesse C, Jones PH, Paluch EK, et al. Membrane Tension Gates ERK-Mediated Regulation of Pluripotent Cell Fate. Cell Stem Cell. 2021;28:273–84.e6.
35. Sigismund S, Confalonieri S, Ciliberto A, Polo S, Scita G, di Fiore PP. Endocytosis and signaling: Cell logistics shape the eukaryotic cell plan. Physiol Rev. 2012;92:273–366.
36. Händel C, Schmidt BUS, Schiller J, Dietrich U, Möhn T, Kießling TR, et al. Cell membrane softening in human breast and cervical cancer cells. N. J Phys. 2015;17:083008.
37. Ren K, Gao J, Han D. AFM Force Relaxation Curve Reveals That the Decrease of Membrane Tension Is the Essential Reason for the Softening of Cancer Cells. Front Cell Dev Biol. 2021;9:1–13.
38. Tsujita K, Satow R, Asada S, Nakamura Y, Arnes L, Sako K, et al. Homeostatic membrane tension constrains cancer cell dissemination by counteracting BAR protein assembly. Nat Commun. 2021;12:5930.
39. Mosesson Y, Mills GB, Yarden Y. Derailed endocytosis: An emerging feature of cancer. Nat Rev Cancer. 2008;8:835–50.
40. Mellman I, Yarden Y. Endocytosis and cancer. Cold Spring Harb Perspect Biol. 2013;5:a016949.
41. Feng Y, Lograsso PV, Defert O, Li R. Rho Kinase (ROCK) Inhibitors and Their Therapeutic Potential. J Med Chem. 2016;59:2269–300.
42. Thottacherry JJ, Kosmalska AJ, Kumar A, Vishen AS, Elosegui-Artola A, Pradhan S, et al. Mechanochemical feedback control of dynamin independent endocytosis modulates membrane tension in adherent cells. Nat Commun. 2018;9:1–14.
43. Ferguson JP, Willy NM, Heidotting SP, Huber SD, Webber MJ, Kural C. Deciphering dynamics of clathrin-mediated endocytosis in a living organism. J Cell Biol. 2016;214:347–58.
44. Gauthier NC, Fardin MA, Roca-Cusachs P, Sheetz MP. Temporary increase in plasma membrane tension coordinates the activation of exocytosis and contraction during cell spreading. Proc Natl Acad Sci USA 2011;108:14467–72.
45. Liu Y, Belkina NV, Park C, Nambiar R, Loughhead SM, Patino-Lopez G, et al. Constitutively active ezrin increases membrane tension, slows migration, and impedes endothelial transmigration of lymphocytes in vivo in mice. Blood. 2012;119:445–53.
46. Rouven Brückner B, Pietuch A, Nehls S, Rother J, Janshoff A. Ezrin is a Major Regulator of Membrane Tension in Epithelial Cells. Sci Rep. 2015;5:14700.
47. Diz-Muñoz A, Krieg M, Bergert M, Ibarlucea-Benitez I, Muller DJ, Paluch E, et al. Control of directed cell migration in vivo by membrane-to-cortex attachment. Harris WA, editor. PLoS Biol. 2010 ;8:e1000544.
48. Diz-Muñoz A, Fletcher DA, Weiner OD. Use the force: membrane tension as an organizer of cell shape and motility. Trends Cell Biol. 2013;23:47–53.
49. Lee KH, Feig C, Tchikov V, Schickel R, Hallas C, Schütze S, et al. The role of receptor internalization in CD95 signaling. EMBO J. 2006;25:1009–23.
50. Kural C, Akatay AA, Gaudin R, Chen BC, Legant WR, Betzig E, et al. Asymmetric formation of coated pits on dorsal and ventral surfaces at the leading edges of motile cells and on protrusions of immobile cells. Mol Biol Cell. 2015;26:2044–53.

51. Aguet F, Upadhyayula S, Gaudin R, Chou Yying, Cocucci E, He K, et al. Membrane dynamics of dividing cells imaged by lattice light-sheet microscopy. Mol Biol Cell. 2016;27:3418–35.
52. Kural C, Tacheva-Grigorova SK, Boulant S, Cocucci E, Baust T, Duarte D, et al. Dynamics of Intracellular Clathrin / AP1- and Clathrin / AP3-Containing Carriers. CellReports. 2012;2:1111–9.
53. Houk AR, Jilkine A, Mejean CO, Boltyanskiy R, Dufresne ER, Angenent SB, et al. Membrane tension maintains cell polarity by confining signals to the leading edge during neutrophil migration. Cell. 2012;148:175–88.
54. McCluskey A, Daniel JA, Hadzic G, Chau N, Clayton EL, Mariana A, et al. Building a better dynasore: the dyngo compounds potently inhibit dynamin and endocytosis. Traffic Cph Den. 2013;14:1272–89.
55. Willy NM, Ferguson JP, Akatay A, Huber S, Djakbarova U, Silahli S, et al. De novo endocytic clathrin coats develop curvature at early stages of their formation. Dev Cell. 2021;56:3146–59.e5.
56. Cakir B, Xiang Y, Tanaka Y, Kural MH, Parent M, Kang YJ, et al. Engineering of human brain organoids with a functional vascular-like system. Nat Methods. 2019;16:1169–75.
57. Elkin SR, Bendris N, Reis CR, Zhou Y, Xie Y, Huffman KE, et al. A systematic analysis reveals heterogeneous changes in the endocytic activities of cancer cells. Cancer Res. 2015;75:4640–50.
58. Sigismund S, Avanzato D, Lanzetti L. Emerging functions of the EGFR in cancer. Mol Oncol. 2018;12:3–20.
59. Schmid SL. Reciprocal regulation of signaling and endocytosis: Implications for the evolving cancer cell. J Cell Biol. 2017;216:2623–32.
60. Polo S, Pece S, Di Fiore PP. Endocytosis and cancer. Curr Opin Cell Biol. 2004;16:156–61.
61. Di Fiore PP. Endocytosis, signaling and cancer, much more than meets the eye. Mol Oncol. 2009;3:273–9.
62. Reis CR, Chen PH, Bendris N, Schmid SL. TRAIL-death receptor endocytosis and apoptosis are selectively regulated by dynamin-1 activation. Proc Natl Acad Sci USA 2017;114:504–9.
63. Schneider-Brachert W, Tchikov V, Neumeyer J, Jakob M, Winoto-Morbach S, Held-Feindt J, et al. Compartmentalization of TNF Receptor 1 Signaling: Internalized TNF Receptosomes as Death Signaling Vesicles. Immunity. 2004;21:415–28.
64. Kohlhaas SL, Craxton A, Sun XM, Pinkoski MJ, Cohen GM. Receptor-mediated Endocytosis Is Not Required for Tumor Necrosis Factor-related Apoptosis-inducing Ligand (TRAIL)-induced Apoptosis. J Biol Chem. 2007;282:12831–41.
65. Austin CD, Lawrence DA, Peden AA, Varfolomeev EE, Totpal K, De Mazière AM, et al. Death-receptor activation halts clathrin-dependent endocytosis. Proc Natl Acad Sci. 2006;103:10283–8.
66. Tanaka M, Itai T, Adachi M, Nagata S. Downregulation of Fas ligand by shedding. Nat Med. 1998;4:31–6.
67. Song E, Chen J, Ouyang N, Su F, Wang M, Heemann U. Soluble Fas ligand released by colon adenocarcinoma cells induces host lymphocyte apoptosis:an active mode of immune evasion in colon cancer. Br J Cancer. 2001;85:1047–54.
68. Schindelin J, Arganda-Carreras I, Frise E, Kaynig V, Longair M, Pietzsch T, et al. Fiji: an open-source platform for biological-image analysis. Nat Methods. 2012;9:676–82.
69. Aguet F, Antonescu CN, Mettlen M, Schmid SL, Danuser G. Advances in Analysis of Low Signal-to-Noise Images Link Dynamin and AP2 to the Functions of an Endocytic Checkpoint. Dev Cell. 2013;26:279–91.
70. Stuart T, Butler A, Hoffman P, Hafemeister C, Papalexi E, Mauck WM, et al. Comprehensive Integration of Single-Cell Data. Cell. 2019;177:1888–1902.e21.
71. Falcon S, Gentleman R. Using GOstats to test gene lists for GO term association. Bioinformatics. 2007;23:257–8.
72. Tanaka Y, Cakir B, Xiang Y, Sullivan GJ, Park IH. Synthetic Analyses of Single-Cell Transcriptomes from Multiple Brain Organoids and Fetal Brain. Cell Rep. 2020;30:1682–89.e3.
73. Tutukova S, Tarabykin V, Hernandez-Miranda LR. The Role of Neurod Genes in Brain Development, Function, and Disease. Front Mol Neurosci. 2021;0:109.

ACKNOWLEDGEMENTS

This work was funded by American Heart Association Postdoctoral Fellowship (17POST33661238) awarded to M.H.K., Pelotonia Fellowship to U.D. and E.T.C., NSF Faculty Early Career Development Program (award number: 1751113) and NIH R01GM127526 to C.K., and NIH R01HL148819 to L.E.N. Any opinions, findings, and conclusions expressed in this material are those of the authors and do not necessarily reflect those of the Pelotonia Fellowship Program or the Ohio State University. We thank Yale Center for Precision Cancer Modeling, for their help with the animal studies, and Yale West Campus Imaging Core. We also thank Dr. Dmitri Kudryashov, Dr. Elena Kudryashova and Junyan Yu from the The Ohio State University for helping us with the viability and apoptosis assays.

AUTHOR CONTRIBUTIONS

MHK oversaw the project, designed, and optimized the experiments and analyzed the data. CK and MHK prepared the manuscript. UD performed the immunofluorescence experiments and analyses in cultured cells, and conducted the viability and cytotoxicity assays involving endocytosis inhibitors. UD and VIA performed the immunofluorescence and flow cytometry assays. BC helped with the organoid experiments. VIA analyzed the organoid images. YT analyzed the single-cell RNA sequence data, YM and EYT performed the tether force experiments. HQ helped with RFP labeling, JP and LRS helped with iPS-derived cardiomyocytes. IP oversaw the organoid experiments, LEN and CK oversaw the project.

COMPETING INTERESTS

L.E.N. is a founder, shareholder, President, and CEO of Humacyte, Inc and serves on Humacyte's Board of Directors. L.E.N.'s spouse is a shareholder of Humacyte. M.H.K, and H.Q. are shareholders and employees of Humacyte, Inc.

ETHICS APPROVAL

All animal studies were carried out in accordance with the Yale University's Institutional Animal Care and Use Committee (IACUC protocol #20218-2021).

ADDITIONAL INFORMATION

Supplementary information The online version contains supplementary material available at https://doi.org/10.1038/s41419-024-06822-3.

Correspondence and requests for materials should be addressed to Mehmet H. Kural, Laura E. Niklason or Comert Kural.

Reprints and permission information is available at http://www.nature.com/reprints

Publisher's note Springer Nature remains neutral with regard to jurisdictional claims in published maps and institutional affiliations.